Cs(Be₂Li)Al₂Si₆O₁₈, a cesium-stuffed host-guest structure, and its structure-property variations with temperature and pressure

Martin Ende [a],[*], G. Diego Gatta [b], Paolo Lotti [b], Alexander Grandtner [a], Ronald Miletich [a]

[a] *Institut für Mineralogie und Kristallographie, Universität Wien, Althanstrasse 14, A-1090, Wien, Austria*
[b] *Dipartimento di Scienze Della Terra, Università Degli Studi di Milano, Via Botticelli 23, I-20133, Milano, Italy*

ARTICLE INFO

ABSTRACT

The solid-state structure of $(Cs,Na)[(Be_2Li)Al_2Si_6O_{18}]$, a beryl-type material, was studied in-situ on single crystal and powder samples at hydrostatic high pressure conditions ($P \leq 9.8$ GPa) as well as under temperature variation ($83 \leq T \leq 1173$ K) by means of Raman spectroscopy, X-ray and synchrotron diffraction. The investigations show an inconspicuous, easily overlooked transformation from $R\overline{3}c$ to non-centrosymmetric $R3c$ space-group symmetry on increasing pressure ($P_c \sim 4$ GPa) and decreasing temperature ($T_c = 312 \pm 5$ K), as revealed by Raman band splitting as well as discontinuities in the evolution of Raman spectra, thermal expansivity coefficients and anomalous compression behavior. Distortions to acentric symmetry originate from the Cs and Na guest atoms inside the channels parallel the c-axis. The occurrence of diffuse scattering planes in all measured data sets indicates substitutional defects inside the channels following an approximate ~4.6 Å periodicity, without any remarkable ordering between adjacent channels. The determined thermal expansivity follows an inverse behavior compared to other beryl-type structures for the $R3c$ phase. The bulk moduli for the two polymorphs compare, together with the observed compressional anisotropy, to other complex beryl-type framework structures. However, the symmetry reduction at high pressure leads to independent displacements of the framework oxygen positions, and as a consequence, to the increase of the coordination number from $[6+6]$ to $[6+9]$ for one of the Cs sites.

1. Introduction

The solid-state properties of microporous framework structures are in the focus of material science since the porosity on a molecular level provides possibilities for various applications, which include functions as microsieves, ion exchangers, catalytic solids, ion and molecule cages or being host materials for nuclear waste disposal e.g. Ref. [1–5]. Apart from physicochemical properties related to the mobility of the extra-framework components, it is the stability of the host framework itself and its resistance to changing conditions that determines the material capability. The beryl-type framework $^{[4]}T1_3\,^{[6]}M_2\,^{[4]}T2_6O_{18}$ (with e.g. T1 = Be, Li; M = Al, Fe, Mg, Sc; T2 = Si, Al) is an outstanding structure because on one hand it does not represent a typical holotetrahedral framework, and on the other hand it has a pronounced one-dimensional microporosity. Representing a heterodesmic (strong, covalent bonds) framework, consisting of both tetrahedral $^{[4]}T$ and octahedral $^{[6]}M$ building units, this host structure reveals separated parallel channels, in a strictly one-dimensional channel system (Fig. S1,

supplement), and therefore has high capabilities for the fixation of extra-framework guest molecules and suitably sized guest atoms, such as here of cesium ions.

The beryl-type framework structure is represented in nature by several (alumino)silicate compounds, for example by beryl ($Be_3Al_2Si_6O_{18}$, space group $P6/mmc$, [6]), bazzite ($Be_3Sc_2Si_6O_{18}$, [7]), stoppaniite ($Be_3Fe_2Si_6O_{18}$, [8]) and cordierite ($Al_3(Mg,Fe)_2AlSi_5O_{18}$, [9–11]). The compounds are known to host inside these pores considerable fractions of M^+ alkali cations and various molecular volatiles (e.g. H_2O, CO_2, or N_2) [1,12]. Most recently, the series of recognized beryl-type $\square_{1-x}M^+_x[^{[4]}T1_3\,^{[6]}M_2\,^{[4]}T2_6O_{18}](m)_y$ solids [$\square$ - vacancy, (m) - extra-framework guest molecule] was extended by $(Cs,Na,H_2O)[(Be_2Li)Al_2Si_6O_{18}]$, which is known even in nature as the gemstone mineral pezzottaite [13–19]. The crystallographic investigations [16,18,19] revealed a rhombohedral superstructure in the space group $R\overline{3}c$, apparently originating from ordering between Li and Be cations on T1 sites. Moreover, the channels inside the stacked six-membered Si_6O_{18} ring units show the highest M^+ content ever located in one of the isostructural
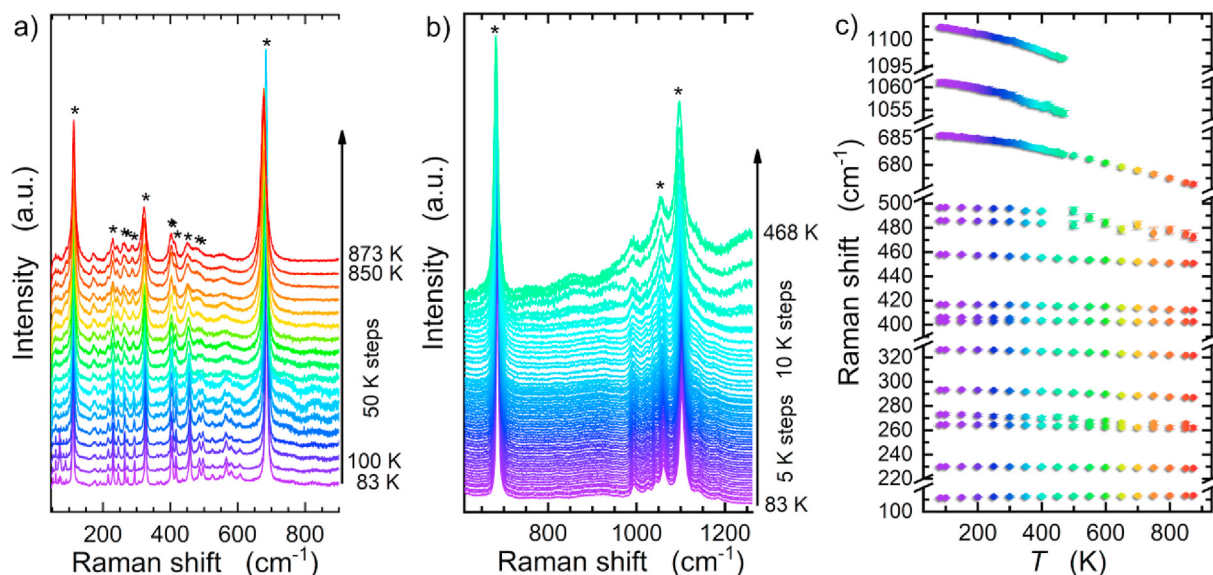
Fig. 1. Sequence of T dependent Raman spectra obtained from a $Cs[(Be_2Li)Al_2Si_6O_{18}]$ single crystal between (a) 83 K and 873 K and (b) 83 K and 468 K. Stars highlight fitted bands plotted in (c), which shows the temperature dependence $\Delta\bar{\nu}/\Delta T$ of the selected Raman bands. Data point colors help to match the corresponding spectra in (a) and (b). (For interpretation of the references to color in this figure legend, the reader is referred to the Web version of this article.)
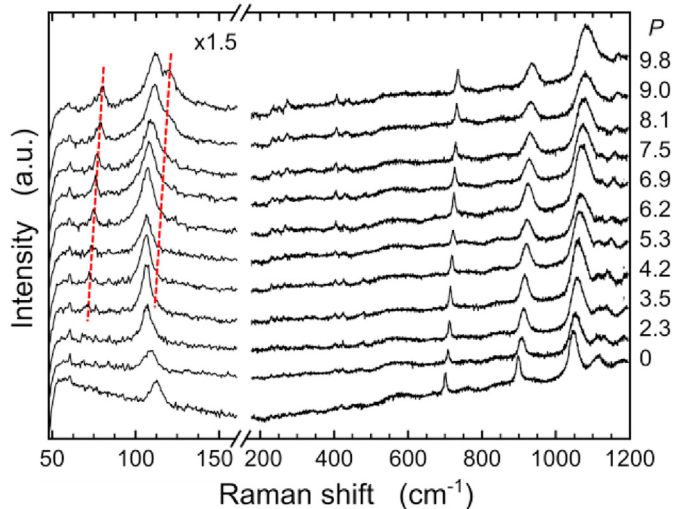

Fig. 2. Sequence of high-P Raman spectra of $Cs[(Be_2Li)Al_2Si_6O_{18}]$ compressed in argon. The scale of the x- and y-axes are changed at the break around 160 cm^{-1}. P is given in GPa. Marked spectral features indicating a potential phase transition occurring between 3.5 and 5.3 GPa.

compounds, which in case of $(Cs,Na)[(Be_2Li)Al_2Si_6O_{18}]$ is required for the charge balance as originating from the distribution of ~1/3 Li^+ and ~2/3 Be^{2+} on the individual T1 sites. Natural samples have been reported often to exhibit deficiency of M^+ guest atoms, which is stoichiometrically compensated by the (Be, Li) substitution on the [4]T1 site, according to the formula $\square_{1-x}M^+_x[(Be_{3-x}Li_x)Al_2Si_6O_{18}]$ [16].

As, in particular, the stuffed channels in $Cs[(Be_2Li)Al_2Si_6O_{18}]$ and the fractions of extra-framework guest atoms inside this open-structure is unique among the beryl-type compounds, the behavior of this material at non-ambient temperature (T) and pressure (P) conditions, and the role played by the channel constituent, was getting into the focus of our interest. Studies on the framework structure of $Al_3(Mg,Fe)_2AlSi_5O_{18}$ revealed anomalous compression under hydrostatic pressure. In detail, an unusual linear volume compressibility was found, while the slope for the interval at low pressure was evolving in a (normal) positive fashion

indicating slightly increasing stiffening, the evolution of bulk modulus for $P > 0.35$ GPa followed a constant line. The same was found for the b- and c-axis, while the a-axis was the less compressible axis and showed conventional stiffening with pressure. For cordierite it was connected to an elastic softening phenomena, as a precursor effect ahead of a supposed structural transition around 6.9 GPa [10,20]. $Al_3(Mg,Fe)_2AlSi_5O_{18}$, a technically prominent ceramic component [21], reveals, among a low thermal expansivity and high resistance to thermal shocks, a pronounced structural stability at high-T conditions, although undergoing an order-disorder transition at high T. This structure type appears to be little influenced in terms of its stability by high degree of energy deposition, neither through high T nor through high irradiation doses [9,11], and is therefore of particular interest as a potential storage material for nuclear waste. $Cs[(Be_2Li)Al_2Si_6O_{18}]$ can contain up to 16 wt% of Cs_2O. In continuation of investigations of structure-property relations, and associated structural phase transitions, on beryl-type analogue phases, we intended to study the elastic behavior of $Cs[(Be_2Li)Al_2Si_6O_{18}]$ under T and P and its deformation mechanisms at the atomic scale, by in-situ measurements. The results of in-situ investigations, by means of X-ray diffraction and Raman spectroscopy on T variations between 83 K and 1173 K (at 1 bar) and isothermal compression up to 9.8 GPa under hydrostatic P conditions at $T = 298$ K, are presented in this study.

2. Methods

2.1. Sample material and sample environment

Single crystals and powder samples were obtained from the same gemstone material from the Sakavalana pegmatite (Madagascar) used by Ref. [18,19], which was structurally and chemically well characterized. The average chemical formula of this sample was therefore determined to Ref. [19]: $(Cs_{0.565}Rb_{0.027}K_{0.017})_{\Sigma 0.600}(Na_{0.101}Ca_{0.024})_{\Sigma 0.125}Be_{2.078}Li_{0.922}$ $(Mg_{0.002}Mn_{0.002}Fe_{0.003}Al_{1.978})_{\Sigma 1.985}(Al_{0.056}Si_{5.944})_{\Sigma 6}O_{18}\cdot 0.27H_2O$. All high-pressure single-crystal investigations were carried out on fragments from a double-sided polished oriented crystal plate (measuring 45 $\pm$ 5 μm in thickness), which was prepared perpendicular to the $hk0$-plane, parallel to the crystallographic c-axis after orientation through X-ray diffraction. All temperature-dependent single-crystal investigations were carried out on crystal fragments with a size around $140 \times 120 \times 40$ μm. Diffuse scattering was demonstrated on an approximately $260 \times 140 \times$

Table 1

Parameters of the single-crystal XRD data collection and results of the structure refinements of rhombohedral $Cs(Be_2Li)Al_2Si_6O_{18}$ ($R\bar{3}c$ or $R3c$, $Z = 18$).

| Pressure/Temperature	173 K	298 K	373 K	473 K	9.13 GPa
Space group	$R\bar{3}c$ (167) [a]	$R\bar{3}c$ (167)	$R\bar{3}c$ (167)	$R\bar{3}c$ (167)	$R3c$ (161)
a (Å)	15.943(9)	15.948(8)	15.950(8)	15.954(8)	15.658(3)
c (Å)	27.808(27)	27.815(25)	27.821(25)	27.829(25)	27.166(6)
V (Å^3)	6121(9)	6126(8)	6130(8)	6135(8)	5768(2)
No. Runs/frames	44/3881	21/2857	23/2504	55/4220	46/3040
Scan time (sec)	50	85	65	55	35
Sample-detector distance (mm)	120	120	60	120	100
No. Measured reflections	111063	43830	110718	64505	20100
No. Unique refl. (all refls., obs. Refls.)	7312, 5732	5818, 5249	7316, 5631	5720, 4932	1707, 1227
max. 2θ (°)	101.2	91.4	101.2	91.4	60.8
R_{int}, R_{sigma} (%)	4.84, 1.80	2.67, 1.31	4.81, 1.64	2.55, 0.99	4.07, 2.64
R_1(obs), R_1(all) (%)	2.73, 4.29	3.13, 2.80	2.99, 4.67	2.54, 3.07	3.54, 5.75
wR_2 (%)	6.68	8.37	7.75	8.05	10.01
GooF	1.05	1.12	1.05	1.07	1.07
obv./rev. Twin fractions	0.93/0.07 [c]	0.70/0.30 [c]	0.90/0.10 [c]	0.69/0.31 [c]	0.41/0.47
					0.06/0.06
Refined/con-/restrained parameters	173/1/0	166/0/0	166/0/0	166/0/0	114/4/0
Weight parameters, a and b [b]	0.026, 9.141	0.043, 5.819	0.033, 6.552	0.045, 3.926	0.055, 10.840
Max/min electron density (e$^-$Å^{-3})	1.416, −0.633	1.916, −0.796	2.114, −0.636	2.012, −0.516	0.711, −0.563

[a] Disordered.

[b] $w = 1/\{\sigma^2(F_o^2) + [a \times P]^2 + b \times P\}$; $P = ([max(0,F_o^2)] + 2 \times F_c^2)/3$.

[c] Two different individuals.
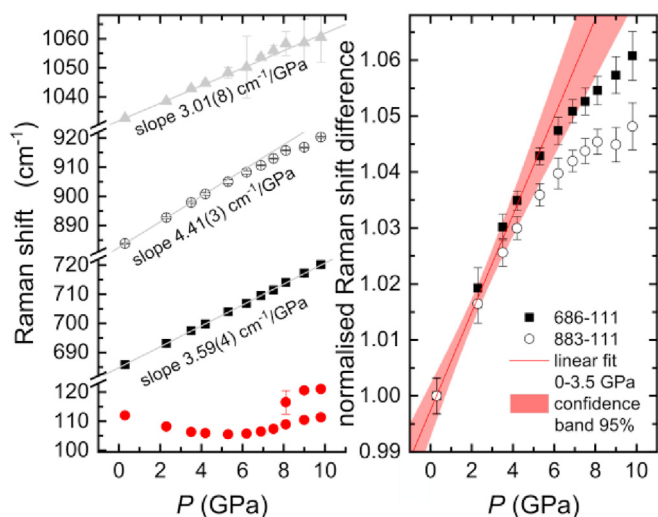
Fig. 3. (a) Pressure dependence $\Delta\bar{\nu}/\Delta P$ of selected prominent Raman bands as obtained from the series of high-P Raman spectra, inclusive the determined slope between 0 and 5 GPa. (b) Differences in Raman shifts between the modes at 686 and 883 cm^{-1}, compared to that at 111 cm^{-1}, provide evidence for a transition between 5 and 6 GPa.

190 μm larger crystal fragment glued to a Kapton loop. High-pressure conditions were achieved in ETH-type diamond anvils cells [22], using anvils with 600 μm culets, conventional steel gaskets with pressure chambers being 250 μm in diameter and a height of 100 μm, and using proper hydrostatic pressure-transmitting media (4:1 methanol-ethanol mixtures for XRD, pure dense argon for Raman spectroscopy). Pressure on isothermal ($T = 298$ K) compression was calibrated using the established quartz and ruby pressure gauges [23–25] to within uncertainties less than ± 0.01 GPa (for quartz) and ±0.07 GPa (for ruby), at 9.13 GPa and if only based on the volume fit uncertainty of around 0.01% [e.g. ± 0.009 Å^3 at 96.780 Å^3], and on the absolute band position error of around 0.005% [e.g. ± 0.5 cm^{-1} at 14404.24 cm^{-1}]), respectively.

2.2. In-situ Raman spectroscopy experiments

Raman spectra at high-P and at T variation between 83 and 873 K were collected by means of a confocal *Horiba Jobin Yvon LabRAM-HR 800* spectrometer using a He–Nd laser source with a wavelength of 632.8 nm for P. For T measurements, a 532 nm constant wave semiconductor laser was used, while the laser power was reduced to 25%. The spectrometer is equipped with an *Olympus BX41* microscope and its *Olympus LMPIanFL* N 50 × objective with a long working distance of 10.6 mm, which enables it to focus the laser beam onto the sample crystal inside the DAC or cooling/heating stage. A total of 61 + 18 Raman spectra at T ranging from 83 to 468 K (Fig. 1a) and 83–873 K (Fig. 1b) were collected, along with a series of 11 high-pressure spectra between 1 bar and 9.8 GPa (Fig. 2), covering a spectral range from 30 to 1300 cm^{-1} Raman shift, at exposure times between 2 × 60 and 3 × 60 s per step for T- and 3 × 40 s per step for P-experiments. For all measurements, a diffraction grating with 1800 lines per mm was used. Spectra were acquired using the *LabSpec 6* software (*HORIBA Scientific*) and *Peakfit v.4* (*Systat Software Inc.*) software was used for background subtraction as well as for the determination of the band position. All Raman spectra were fitted with the Gauss-Lorentz-area method.

2.3. In-situ X-ray diffraction experiments

XRD intensity data collections were performed using a Stoe StadiVari diffractometer (equipped with a Dectris Pilatus 300 K detector with a 450 μm silicon layer, an air-cooled Incoatec IμS molybdenum microfocus tube operated at 50 kV/1 mA, beam diameter of ~110 μm FWHM) and a 120 mm sample-detector distance. In-situ measurements at 473 K, 373 K, 298 K, and 173 K were performed using an Oxford CryoSystems nitrogen-gas Cryostream cooler, with resistive heating at a temperature stability of the N$_2$ flow of around 0.1 K on two single crystal samples. In-situ high-pressure data were collected from a ~150 × 120 × 45 μm sample crystal (Fig. S2, supplement). XRD intensity data were collected at $2\theta \leq 92°$, performing 0.5° ω-scan at 50 s of exposure time per frame. The diffraction patterns were indexed and intensities integrated using the X-area 1.72 software (Stoe & Cie GmbH). Integrated intensities were corrected for absorption effects, through DAC components and sample, by using the ABSORB code [26]. Crystal structures were refined using neutral scattering curves from the International Tables for Crystallography [27] with
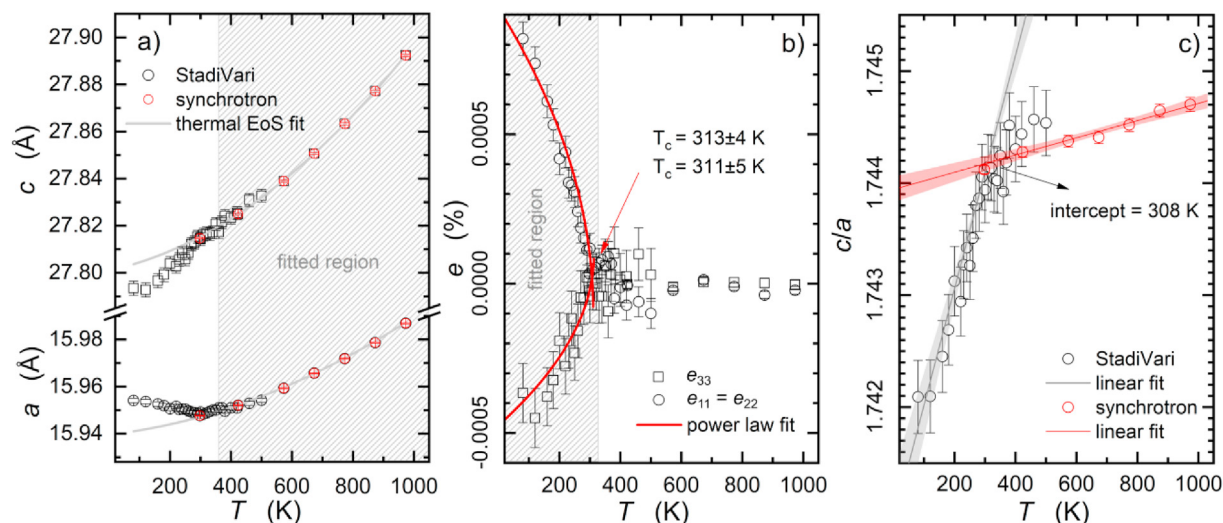
Fig. 4. (a) Temperature-dependent evolution of the unit-cell lengths along a and c. The grey lines correspond to fits after Berman 1988. (b) Corresponding spontaneous strain components derived from the T-dependent lattice parameters a (e_{11}) and c (e_{33}) using the extrapolated thermal EoS fit as baseline and for example the formula $e_{11} = (a - a_0)/a_0$. Red lines indicate power law fits, with a critical exponent of 0.5, typical for second-order phase transitions. These fits were used to get an indication of the transition temperature (T_c). (c) T-dependent evolution of the c/a ratio including linear fits (grey line: $T = 100–350$ K, red line: $T = 400–973$ K) with 95% confidence bands intersecting at 308 K. (For interpretation of the references to color in this figure legend, the reader is referred to the Web version of this article.)

Table 2
Elastic properties and corresponding bulk moduli for the unit-cell volume V and the lattice parameters along directions a and c, as obtained from fitting third-order Birch-Murnaghan EoS and a thermal EoS after Berman (1988) to the respective T/P–V, T/P-a, and T/P-c data sets.

	V_0, a_0, c_0	K_0, M_0 (GPa)	K', M'
0–9.1 GPa	$V_0 = 6143.1(4)$ Å^3	152.3(1.0)	−1.1(2)
	$a_0 = 15.9608(1)$ Å	495(4)	−3.2(7)
	$c_0 = 27.8465(4)$ Å	387(6)	−2.6(8)
0–3 GPa	$V_0 = 6143.8(7)$ Å^3	144.6(2.2)	4 [a]
	$a_0 = 15.9615(6)$ Å	472(8)	12 [a]
	$c_0 = 27.8456(3)$ Å	373(6)	12 [a]
4–9.1 GPa	$V_0 = 6182(3)$ Å^3	115.4(1.2)	4 [a]
	$a_0 = 15.9883(47)$ Å	387(9)	12 [a]
	$c_0 = 27.9239(59)$ Å	285(4)	12 [a]
	V_0, a_0, c_0	α_0 ($\times 10^{-6}$ K^{-1})	α_1 ($\times 10^{-8}$ K^{-2})
80–300 K [b]	$V_0 = 6127.0(6)$ Å^3	0.71(11)	0 [a]
	$a_0 = 15.9500(5)$ Å	−1.65(47)	0 [a]
	$c_0 = 27.8085(15)$ Å	4.0(8)	0 [a]
300–973 K [b]	$V_0 = 6126.1(3)$ Å^3	6.9(3)	1.4(8)
	$a_0 = 15.9471(4)$ Å	2.24(14)	0.43(4)
	$c_0 = 27.8152(8)$ Å	2.48(17)	0.49(4)

[a] Implied value.
[b] T_{ref} for both T-ranges = 298 K.

SHELXL [28] and the graphical user interface ShelXle [29]. Details of the individual data collections are summarized in Table 1.

The unit-cell parameters and their variations with pressure were determined from measurements on a Stoe AED II diffractometer (Eulerian cradle, graphite-monochromatized Mo-radiation from 50 kV/30 mA sealed-tube source, point detector). Data acquisition and refinement was performed using the SINGLE software [30]. In addition to the sample crystal (~150 × 120 × 45 µm), a quartz single crystal (~160 × 80 × 40 µm) was added in the pressure-chamber of the DAC and its unit-cell parameters were measured for precise pressure determination. Applying the 8-position centring mode [31], both unconstrained and symmetry-constrained unit-cell parameters were determined for 12 pressure points in the range between 10^{-4} GPa and 9.13 GPa at $T = 298$ K (Table S1). Equation-of-state (EoS) parameters were fitted using the software EoSFit7GUI [32].
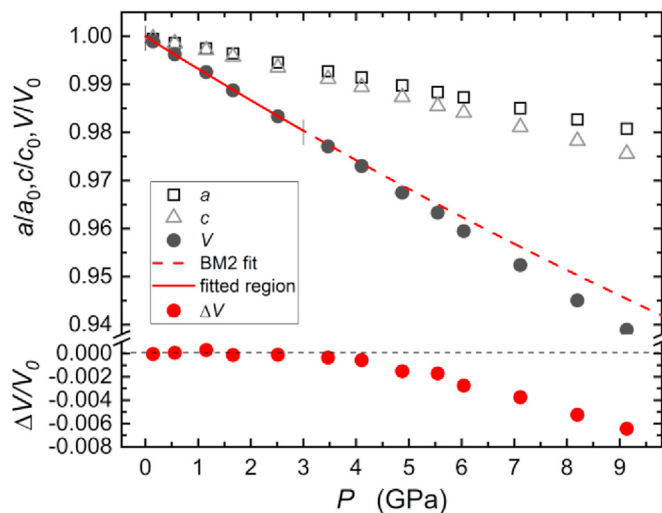
Fig. 5. Pressure-dependent evolution of the unit-cell parameters. The red line corresponds to a fit of BM-2 EoS up to 3 GPa, with the respective parameters for the axial moduli as listed in Table 2. (For interpretation of the references to color in this figure legend, the reader is referred to the Web version of this article.)

2.4. Synchrotron X-ray powder diffraction experiments

In-situ high-temperature powder X-ray diffraction data were collected at the MCX beamline at ELETTRA (Trieste, Italy) using a Huber 4-circle goniometer, focussed beam conditions, and double slit in front of a point detector. Powder samples were contained in a quartz-glass capillary. The use of a gas blower (*Oxford Danfysik DGB-0002*) allowed to control the temperature up to 1273 K (±2 K). X-ray powder diffraction patterns were collected with a monochromatic beam of 0.7750 Å, and diffraction data were analysed by Le Bail method [33] to obtain precise unit-cell parameters in the temperature range between 298 and 1173 K. For the full-profile fit, the GSAS package [34,35] was used (profile function: pseudo-Voigt; background function: Chebyshev polynomial).
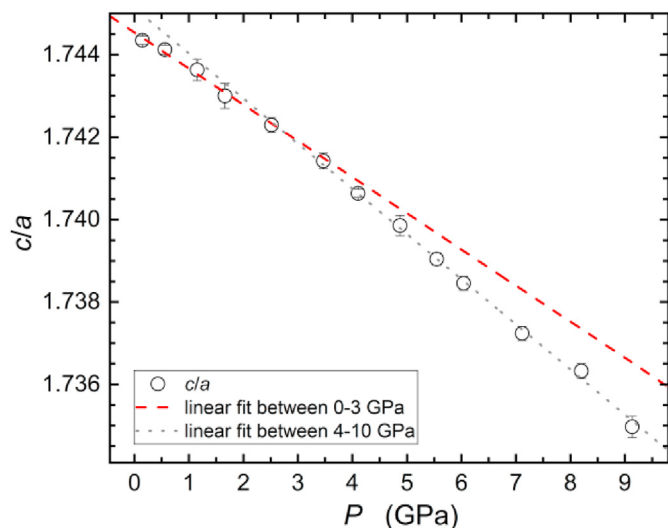
Fig. 6. Pressure-dependent evolution of the c/a ratio, including linear fits intersecting each other at about 2.8 GPa.

3. Results

3.1. In-situ Raman spectra under T and P variation

The vibrational properties of $Cs[(Be_2Li)Al_2Si_6O_{18}]$ have been investigated in detail by Refs. [19], who identified $44 A_{1g} + 92 E_g$ theoretically possible active Raman modes. The most characteristic Raman bands reported so far correspond to those observed within the wavenumber range $50-1300$ cm^{-1}. In the following experiment we concentrated on 15 bands located at $112(s)$, 230, 265, 272, 293, 326(s), $403 + 405$, 416, 456, 485, 498, 685(s), 1058(s) and 1100(s) cm^{-1} at ambient conditions (s – strong Raman band, cf. Fig. 1). The modes below 300 cm^{-1} are attributed to rotation and breathing of the Si_6O_{18} ring [36,37]. The intense peaks at $403 + 406$ cm^{-1} may be ascribed to deformation of the ring units [38], while the strong peak at 685 cm^{-1} has been assigned to the stretching vibration of the ring unit, coupled to the Be–O stretching mode [19]. The Raman spectrum is dominated by a strong mode at 1100 cm^{-1}, which corresponds to the Si–O stretching mode, as pointed out by previous studies (cf. [19] and references therein).

The series of spectra under T variation (Fig. 1) show no apparent changes with respect to the number, position and intensity of the observed peaks. It is evident that the $Cs[(Be_2Li)Al_2Si_6O_{18}]$ structure, in terms of arrangement of the building units and their local symmetries, remains substantially unchanged across the T-range investigated. The evolution of spectra does not provide any hint of a phase transition. The only clear changes concern a gradual broadening of the peaks (Fig. S3, Supplement) in accordance with increasing lattice dynamics, as can be seen from the increase in the FWHM's from ~3 to 5 cm^{-1} at 83 K to ~10

to 20 cm^{-1} at 873 K. If band positions are plotted (Fig. 1c), the typical redshift to be expected for increasing T can be observed. It is noteworthy, however, that two separate ranges of linear trends, with different slopes, can be traced for individual Raman bands, with a smooth and apparently continuous transition approaching room temperature (RT).

An additional series of spectra was collected on an isothermally compressed sample at RT under quasi-hydrostatic conditions using argon as the pressure-transmitting medium. The sequence of in total 11 high-pressure Raman spectra, recorded up to 9.8 GPa, also shows no substantial changes, which would reflect structural modifications. The prominent Raman bands attributed to the vibrational modes of individual framework building units show no deviations from an almost linear blueshift trend. Deviations from linear trends are only discernible in the low-frequency range of the spectrum (Figs. 2 and 3), e.g. for the band at ~111 cm^{-1}. This band shows a redshift up to ~3 GPa, followed by a blueshift beyond ~5.3 GPa, which is accompanied by a band splitting with a shoulder emerging on the high-energy side of the band. By evaluating the relative differences in Raman shifts, a critical pressure P_c can be determined around 5.3 GPa. The changes at a pressure beyond P_c involve even new bands, e.g. that one at ~75 cm^{-1} (cf. Fig. 2). Since bands in this range of low energy vibrational and rotational modes can be attributed to the weak bonds of highly coordinated atoms, it can be assumed that these supposed changes might affect the arrangement of the (extra-framework) channel population.

3.2. Thermo-elastic behaviour

A series of 27 precise lattice parameters in hexagonal setting was determined from single-crystal X-ray diffraction between 83 and 500 K, in addition to 7 data points extracted from synchrotron powder data collected between 298 and 1173 K (Tables S2 and S3). The evolution of the unit-cell parameters with T confirmed that, within the T-range investigated, the rhombohedral cell, previously reported for pezzottaite at room conditions [18], is preserved. However, the variation of unit-cell edge lengths along [100] and [001] suggests a change at ~308 K, where temperature dependencies exhibit different slopes (Fig. 4). Using a linear approximation for the data up to ~300 K, or a simple extension after [39] to accommodate non-linear expansion for the high-T range, yield the coefficients as summarized in Table 2 (fits to the experimental data were done with EoSFit7GUI [32]). The negative thermal expansion coefficient along the a-axis direction ($\alpha = -1.65 \pm 0.47 \times 10^{-6}$ K^{-1} at $T = 250$ K) is remarkable for the low-T range, whereas for $T > T_c$ a clearly positive value for the thermal expansion coefficient ($\alpha = 2.50 \pm 0.12 \times 10^{-6}$ K^{-1} at $T = 350$ K) is obtained. A slight decrease in the values for α can be obtained along the c-axis direction at increasing T, though keeping positive values ($\alpha = 4.0 \pm 0.8 \times 10^{-6}$ K^{-1} for $T = 250$ K, $\alpha = 2.73 \pm 0.15 \times 10^{-6}$ K^{-1} for $T = 350$ K). The significant change observed along the direction parallel to (//) [100] also considerably affects the c/a ratio by increasing the slope from constantly around $7.7(8) \times 10^{-7}$ K^{-1} between room temperature and 1000 K to about 1.0×10^{-5} K^{-1} between 100 K

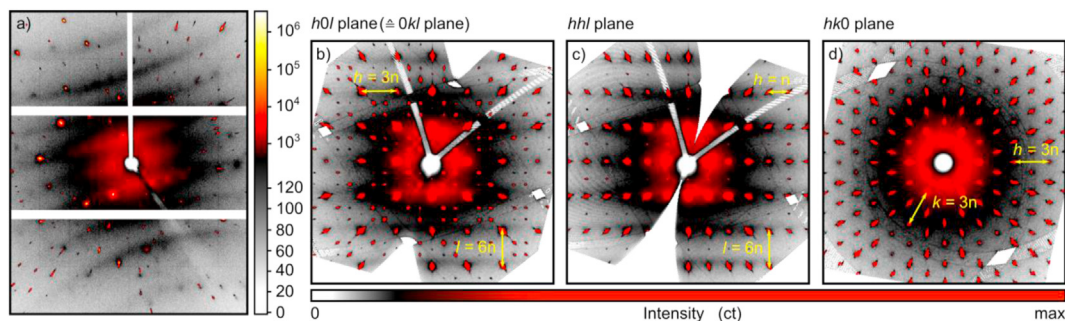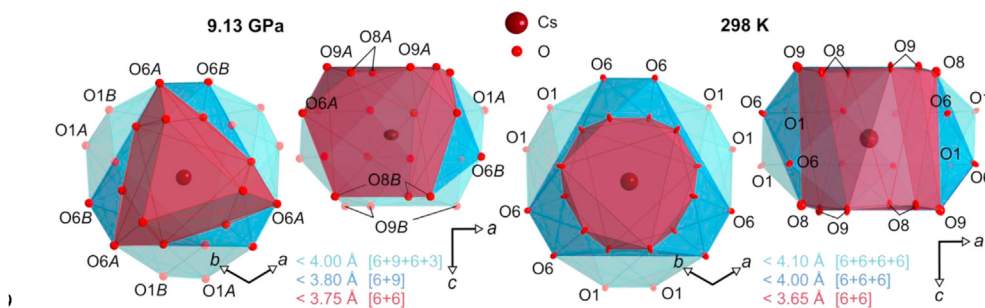**Fig. 7.** XRD diffuse scattering in $Cs[(Be_2Li)Al_2Si_6O_{18}]$ at 298 K. (a) Single-frame oscillation photography ($\Phi = 0.5°$) exposed for 300s. (b–d) Selected layers out of the reconstructed reciprocal space according to the layers $h0l$, hhl and $hk0$.

Fig. 8. Arrangement of Na and Cs sites within a single channel along the *c*-axis (between z = 0 and z = 1). Electron densities correspond to the maps calculated from the data collected at 173 K. Na1, Na2*A*, Na2*B*, Cs1 and Cs2 positions correspond to the refined site. Cs1* and Cs2* are the theoretical central positions on the triad; Na2* is the mean position that splits into Na2*A* and Na2*B*. The presumable Ow positions (i.e. Ow1 and Ow2) are necessary for the completion of the Na coordination, but their positions superimpose with Cs sites and have not been resolved. It is remarkable that the atom distribution follows multiples *n* of 1/12 along the *z*-coordinate inside the channels.

and RT (Fig. 4). From the intersections of the respective empirically determined curves shown in Fig. 4, individual values of 311 ± 4 and 314 ± 5 K can be derived for the critical temperature T_c. The discontinuity can also be seen in the evolution of the unit-cell volume, with a considerably smaller volume expansion below T_c compared to that above T_c (Table 2).

Beryl-type framework structures were found to have, in general, a low thermal expansivity (e.g. $+2.0 \times 10^{-6}$ K^{-1} for polycrystalline cordierite ceramics [40]), usually with axial expansion along the *c*-axis showing small or even negative values $\{+2.6 \pm 0.1 \times 10^{-6}$ K$^{-1}//a$ and $-2.9 \pm 0.4 \times 10^{-6}$ K$^{-1}//c$ in Be$_3$Al$_2$Si$_6$O$_{18}$ (beryl); $1.7 \pm 0.1 \times 10^{-6}$ K$^{-1}//a$ and $+0.16 \pm 0.60 \times 10^{-6}$ K$^{-1}//c$ Be$_3$(Al,Cr^{3+})$_2$Si$_6$O$_{18}$ (emerald) after [41]; $+3.3 \times 10^{-6}$ K$^{-1}//a$, $+2.7 \times 10^{-6}$ K$^{-1}//b$ and -1.2×10^{-6} K$^{-1}//c$ in Al$_3$Mg$_2$AlSi$_5$O$_{18}$ (cordierite) after [42]$\}$. The expansion of any given beryl-type framework depends on the *T* response of the framework itself involving T–O–T and O–T–O angular changes, the expansion coefficients of the non-tetrahedral bonds, and the interplay between these two factors [43]. The thermal expansivity of Cs[(Be$_2$Li)Al$_2$Si$_6$O$_{18}$] above T_c (Table 2) is comparably low, being similar in isotypical framework materials, mentioned above. Nevertheless, the anisotropy of thermal expansion was found to be less pronounced as the two main components of the α_{ij} tensor reveal positive values, at least for the *T* range between 300 and 973 K. A negative thermal expansion value has indeed been observed for the phase at *T* < 300 K, but it affects, the first time reported for any beryl-derived structures, the *a*-axis direction.

Fig. 9. Various theoretical ordering schemes within a single channel along the *c*-axis, with: (a) only Cs atoms; (b) only Na atoms; (c) 75% Cs and 25% Na atoms; (d) 80% Cs and 20% Na atoms, whereby the whole possible occupation is 100% for (a) and (b), 75% for (c) and 83.3% for (d) (measured: ~86.6%). The ratio of Cs/Na is 2 and 4 for (c) and (d) respectively (measured: ~5.4).

3.3. Isothermal compressibility and equation of state

The unit-cell parameters measured at different *P* are summarized in Table S1. The least-squares refinements of base vectors were performed in a first step with symmetry-unconstrained parameters in a triclinic setting, in order to determine possible pseudo-symmetries as due to symmetry breaking associated with any structural transition. The symmetry-unconstrained refinements confirmed the hexagonal setting of base vectors with *a* being equal to *b* within the experimental uncertainties, and the angles α, β, and γ showing values close to 90° and 120°, respectively.

The *P* dependency of unit-cell parameters (Fig. 5) reveals a compressional anisotropy similar to that reported for other beryl-type materials, with the structure being ≈ 22% less compressible along the *a*-axis than along the *c*-axis [9–11,44,45]. A careful inspection of the *P* dependencies shows that both axial and volume compressibilities increase at elevated *P*, although at increasing density one can usually expect opposite trends. Fitting a Birch-Murnaghan EoS [46] to the experimental data (Table 2, Fig. S4 in the supplement), the pressure derivatives of the moduli *K* (for volume) and *M* (axial) show negative values, i.e. $M' = dM/dP$ for *a* and *c* is -3.8 ± 0.8 and -2.8 ± 0.6, $K' = dK/dP$ for *V* is -1.17 ± 0.14. Axial negative values have been previously reported for irradiated and non-irradiated cordierite [9–11], while a study on beryl itself did not report any anomalous behaviour [44]. Structural instabilities have been reported for isostructural frameworks suggesting in Be$_3$Al$_2$Si$_6$O$_{18}$ and Al$_3$(Mg,Fe)$_2$AlSi$_5$O$_{18}$ transformations to intensively twinned or gently modulated polymorphs of lower symmetry [9,10,20,45]. Thus, the remarkable elastic-softening behaviour in Cs [(Be$_2$Li)Al$_2$Si$_6$O$_{18}$] can be interpreted as a precursor of an impending polymorphic transition at *P* beyond those achieved in this study.

The fit with a third-order Birch-Murnaghan EoS to the volume data across the entire *P* range (Fig. S4, supplement) provides a bulk modulus

Fig. 10. Coordination polyhedra around Cs2 positions at 298 and 9.13 GPa illustrating the changed coordination of the cesium atom from approximately [6 + 6] coordination at ambient conditions to [6 + 9] at high-*P*. The high-*P* bonding configuration is not only the result of three further atoms (O6*A*), but a substitution of O9*B* atoms for O6*A* and O6*B* atoms. The O1 atoms where not influenced in that way, but clearly split up to O1*B* (3.88(2) Å Cs–O distance) and O1*A* (3.98(2) Å Cs–O distance).

of 152.4 ± 0.8 GPa, which follows the Anderson-Anderson relationship (Anderson and Anderson, 1970) falling at a given volume V_0 per formula unit Z with $V_0/Z = 341.31$ Å^3 between those for Be$_3$Al$_2$Si$_6$O$_{18}$ ($K_0 = 180.2$ GPa, $V_0/Z = 337.75$ Å^3, [44]) and Al$_3$(Mg,Fe)$_2$AlSi$_5$O$_{18}$ ($K_0 = 131.1$ GPa, $V_0/Z = 387.92$ Å^3, [10]). Nevertheless, the careful inspection of the residuals (cf. Fig. S5, supplement), as calculated from the differences between the experimental unit-cell volume and the theoretical one derived from the EoS fit, gives a hint for deviations in the proximity of ~3–4 GPa. Deviations ΔV reach almost ~3 Å^3, compared to 0.5 to 0.9 Å^3 at $P < 3$ GPa. While the residuals for the EoS fit across the entire pressure range (0–9 GPa) might be not that suspicious, the truncation of the pressure-range fit at the critical pressure between 3 and 4 GPa provides a much clearer picture (Fig. 5). Although the EoS fits for the 0–3 GPa range can not be performed with unconstrained pressure derivatives for the bulk moduli, the obtained results are realistic (Table 2), and provide a sufficient explanation for the earlier discussed negative vales for K' and M'. The occurrence of an apparently continuous structural change, which can be interpreted as a weak second-order transformation, is also supported by the axial compressional trends along [100] and [001] and in particular by the c/a ratio (Fig. 6).

3.4. Structure evolution at non-ambient conditions

All the X-ray diffraction patterns collected in this study at non-ambient conditions (i.e. 173 ± 1 K, 298 ± 2 K, 373 ± 1 K, and 473 ± 1 K at 1 bar; 9.13 ± 0.07 GPa at 298 K) show reflection conditions conforming to Laue class $\bar{3}m1$, with the possible space groups $R\bar{3}c$ (no.167) and $R3c$ (no. 161), in one of the two possible rhombohedral orientations following obverse and reverse settings.

Diffraction images recorded at different temperatures shows weak but recognizable diffuse scattering (Fig. 7), which is independent of the temperature (Fig. S6, supplement). The appearance of the diffuse scattering corresponds to disk-like intensity distributions in reciprocal space, with the disks arranged along the c^* direction. Since, single detector frames show only a plane cut through the reciprocal space, these disks appear either imperceptible or as broad diffuse lines (Fig. 7a), which in contrast to diffuse planes parallel to (001) clearly lose intensity with rising 2θ angle. The scattering features occur with maximum intensities at multiples of $l = 6n$ (Fig. 7), in analogy to the ~4.6 Å spacings (corresponding to the Cs···Cs distance within the channels). The scattering intensity within these disks is radially symmetrical within reciprocal layers parallel to $hk0$ (Fig. 7), with gradually decreasing intensity with increasing scattering vector s or q (commonly used in aperiodic crystallography as q-vector). Note that the q-vector is used here rather in terms of its length, which is defined using the wavelength (λ) and scattering angle (θ) as q = $4\pi \cdot \sin(\theta)/\lambda$. In contrast, rational (1/4) or irrational (0.26789) fractions of hkl are commonly used for q (modulation wave vector) to describe commensurate or incommensurate modulated crystal structures. This occurrence suggests one-dimensional substitutional disorder (e.g. Cs1, Cs2 and Ow1, Ow2) of extra-framework population along the channel direction, which are quite ordered along the c-direction and which, in their lateral arrangement, should be arranged independently of one another.

The structure refinements based on the integrated Bragg peaks was attempted for all data sets using the structure model reported by Ref. [16, 18], with fully occupied framework positions and corresponding partial site occupation for the extra-framework atoms Cs and Na. After a careful inspection of the electron-density maps, it was not possible to clearly identify (and refine) the extra-framework positions ascribed to H$_2$O (Ow1 and Ow2), reported as O10 and O11 by Ref. [16], from superimposing Cs2 and Cs1 sites. Exceptionally large and systematically increased values for weighting factors, as well as of the several anisotropic displacements parameters (in particular those of Cs, Na, Li, Be and some oxygen positions), gave reason to carry out comparative symmetry evaluations, using the tools provided by the *Bilbao Crystallographic Server* [47–49]. In particular, the data sets at 173 K and 9.13 GPa revealed also small but significant oxygen atom displacements (with similar orientation) for the same type of atoms (cf. Fig. S7 in the supplement), pointing out the true symmetry could be non-centrosymmetric $R3c$ rather than centrosymmetric $R\bar{3}c$.

Based on previous crystallographic discussions on twinning and on the presence of acentric twin domains in pezzottaite crystals [18], the distribution statistics of normalized structure factors were also carefully checked. The evaluation of the N(Z) distribution suggests, along with the Flack test [50], a high likeliness for centrosymmetry, but the occurrence of reticular merohedry and twinning (with obverse and reverse domains, cf. Fig. S8 in the supplement) raised doubts about the reliability of the results. For example, the ambiguous value for the Flack x parameter (i.e. 0.38 ± 0.04 at 173 K and 0.40 ± 0.11 at 9.13 GPa) is likely affected by the presence of merohedral twinning [51]. Accordingly, all structure refinements were carried out in both potential space groups ($R\bar{3}c$ and $R3c$), taking into account the possible twin laws (with obverse/reverse domains) and the twinning due to the loss of the inversion centre (i.e. two twin domains in $R\bar{3}c$, four domains in $R3c$). Of course, lower residuals have been obtained for the *T*-series datasets and the high-*P* dataset at 9.13 GPa with refinements in the acentric space group $R3c$, but much more significant is that the b weighting parameter in SHELX for the high-*P* dataset was lowered dramatically (decreased by 60%). The residuals and further fit parameters also from using MERG0 and a fit with anisotropically refined Si and Al atoms (lowering the b value as well) are shown in the supplement (Table S4). The refinements of the series (taken with two crystals) under *T* variation yield reasonable scale factors for the four twin fractions, with approximately equal proportions of the oppositely acentric domains, i.e. with 43% and 46% at 9.13 GPa (cf. Table 1).

For the data collections at 298 K, 373 K and 473 K, the refinements in $R3c$ were less stable, the weighting parameters were inconspicuous and the differences in atom position between $R\bar{3}c$ and $R3c$ within the 3 sigma level (Fig. S5). Therefore, these data sets were refined in centrosymmetric $R\bar{3}c$, with only two-individual twin fractions corresponding to the domains in obverse and reverse rhombohedral settings. The situation was slightly different at 173 K. The refinement using space group $R\bar{3}c$ produces a high weighting parameter b of 12.964 (a = 0.026). As the violation of centrosymmetric symmetry seemed to affect only a few atoms (Fig. S5), even the data set collected at 173 K was finally refined in

M. Ende et al.

$R\overline{3}c$, using a structure model with disordered O3, O5 and Na2 positions. This already lowered the value of the *b* parameter in the weighting to 9.141 while the parameter *a* retains at 0.026. However, up to a value of around 5–6, for such a natural and huge structure with multiple site occupations, the *b* value is not considered to be crucial. On the other hand, it is a further sign that the chosen space group $R\overline{3}c$ is likely not the right choice to account for the symmetry of the channel content and nearby atom positions at 173 K. Changing from the *R3c* to the disordered $R\overline{3}c$ structure also lowered other parameters (R$_1$[obs]: 2.86–2.73; R$_1$[all]: 4.29–4.43; wR$_2$: 7.15–6.68; highest difference peak: 1.536 e$^-$Å^{-3} – 1.416 e$^-$Å^{-3}; deepest hole: -0.793 e$^-$Å^{-3} – -0.633 e$^-$Å^{-3}). It is noteworthy that the site-occupation factors (SOF's) of the split positions correspond in pairs to a ratio of 0.9 : 0.1, which in turn corresponds to the refined twin fractions of two oppositely acentric domains. Although weak electron densities (<1.4 e$^-$ Å^{-3}, 173 K) have been localized in the vicinity of the Cs atoms, and could not be unambiguously ascribed to the partial occupied Ow positions as proposed by Refs. [16], the final refinements of the data sets collected under *T* variation were carried out only with Na and Cs extra-framework population. However, the electron-density distribution around the average Cs positions located at the central sites 6*a* and 12*c*, and the ADP's for atoms refined at 0,0,*z*, suggest a small but considerable lateral displacement off the three-fold axis. Thus, the final refinements of the data sets collected under *T* variation were carried out accordingly with atoms at general positions with respective SOF's listed in Tables S5 to S8 and S10 to S13.

At high pressure, the Cs atoms were localized directly on the threefold axis, due to the reduced accessible reciprocal space. However, large isotropic displacement factors were observed for the Cs sites. In particular, this phenomenon is pronounced for the Cs2 site (U_{iso} of 0.037 Å^2), if compared to the Si atoms (U_{iso} of 0.006 Å^2), which results in a root-mean-square value for the atomic displacements of 0.19 Å (Cs2) and 0.08 Å (Si). As for the low-*T* structure, the refinement was first done using the $R\overline{3}c$ space group, resulting again in large values for the weighting factors and large displacement parameters for several atoms. Any attempt to test the non-centrosymmetry failed due to the lack of a sufficient number of Friedel pairs (Friedel coverage is 47.5%), which in turn is due to the limitation of the accessible reciprocal space for high-*P* measurements in a DAC. However, for a refinement in $R\overline{3}c$, the findings suggested a plausibly large splitting of oxygen position, supporting the refinement of the high-*P* structure in the non-centrosymmetric space group *R3c* (cf. Table S9).

4. Discussion

4.1. Host framework and its variations at non-ambient P and T conditions

The [(Be$_2$Li)Al$_2$Si$_6$O$_{18}$]$^-$ host framework with its ideal symmetry $R\overline{3}c$ can be derived by Li and Be ordering at the $^{[4]}$T1 position in the beryl-type [$^{[4]}$T1$_3$ $^{[6]}$M$_2$ $^{[4]}$T2$_6$O$_{18}$] framework (*P6/mcc*), with fully occupied Al on $^{[6]}$M and Si on $^{[4]}$T2. The refinements of this study confirm, for any data set measured at non-ambient *P,T* conditions, the cation distribution as previously described for pezzottaite [16,18,19], with Li at the 18*e* and Be at the 36*f* Wyckoff positions in $R\overline{3}c$. Symmetry lowering according to $R\overline{3}c \rightarrow R3c$ leads to a distribution on three non-equivalent 18*b* sites in *R3c* (Li, Be*A*, Be*B*). Apart from the Be site, all Si and oxygen positions split into two independent sets (labeled *A* and *B*: Si1, Si2, Si3 in $R\overline{3}c \rightarrow$ Si1*A*, Si1*B*, Si2*A*, Si2*B*, Si3*A*, Si3*B* in *R3c*), originating from the loss of the center of symmetry.

Nevertheless, Raman spectra do not provide any clear evidence for the theoretically possible splitting of the relevant T-O vibration bands at low-*T*, and all bands in the relevant wavenumber range between 900 and 1200 cm^{-1} remain apparently unchanged across the entire *T* range (cf. Figs. 1 and 2), in terms of possible splitting, emerging of shoulders, or peak broadening. A plausible explanation for this would be that the individual tetrahedral units do not show such large differences at different

T. Their vibration frequencies are, therefore, remarkably similar, and the actual changes due to the reduction in symmetry only manifest themselves in relative displacements of the TO$_4$ units within the framework. Accordingly, the only recognizable changes can be seen in the low-frequency spectral range, in which the external vibrations and breathing modes can be observed.

Changes due to the applied pressure, on the other hand, show a broadening of these modes that can be assigned to the diversification of T-O vibrations, as well as emerging and splitting at *P* greater than 3 GPa (i.e. bands at 75 and 111 cm^{-1}, cf. Figs. 2 and 3). Especially this splitting could be due to the increase of Raman active modes attributed to Cs, which occupies two different Wyckoff positions, 12*c* and 6*a* at $R\overline{3}c$ (four possible Raman active modes) and three times the Wyckoff position 6*a* at *R3c* (nine possible Raman active modes, [52]). Moreover, the *P*-induced distortions of the structure are comparably larger than the *T*-related ones. In addition, the displacive framework distortions are subjected to other mechanisms owing to the interaction between framework and extra-framework population.

Nevertheless, the change in the *P* dependence of the band positions is an indication of the assumed change in symmetry. This is also manifested in the variation of *T*-dependent unit-cell parameters (cf. Fig. 4), which are only marginal but noticeable as exemplified by the *c/a* ratio (cf. Fig. 4). Since both structures in $R\overline{3}c$ and *R3c* remain substantially unchanged, most of the essential symmetry elements are preserved, and only the loss of the center of symmetry leads to the observable differences. Intersecting trends in Figs. 5 and 7 provide values of approximately 2.8 GPa for the critical transition pressure *P*$_c$ referring to the $R\overline{3}c \rightarrow R3c$ transition on compression, and approximately 308 K for the $R3c \rightarrow R\overline{3}c$ counterpart on *T*-increase *T*$_c$. Regardless of the *P* or *T* being the tuneable property, the *c/a* ratio decreases or increases for both structures in the same way, always with a steeper slope for the non-centrosymmetric *R3c* phase (Figs. 5 and 7).

The most unexpected property of pezzottaite is the fact that it does not exhibit a negative expansion on *T* increase along the *c*-direction and shows, in contrast, the largest positive value determined for the α$_3$ coefficient, if compared to any isotypic material. On the other hand, even negative α$_1$ values can be observed for the low-*T* phase of Cs[(Be$_2$Li)Al$_2$Si$_6$O$_{18}$].

This inverse behavior can only be attributed to the fact that this framework structure must accommodate extra-framework atoms intercalated inside the channels. With the placement of those guest atoms, volume optimization within the channels can be achieved only by stretching along the *c*-axis. That would also be plausible, especially since the channels at R*T* appear too wide for the Cs atoms (evidence of displacement off the triad were reported). The increasing vibration dynamics with *T* enables the Cs atoms to take up the more central position, which in turn reduces the lateral channel diameter, but takes up more space in the *c*-direction. The compressional anisotropy is apparently less dependent on the type and fraction of channel constituents, and the presence of C*s* atoms does not seem to have a strong influence on the high-*P* properties of this framework type. The compressibility along the *c*-axis is about 25–30% higher of all the other investigated isotypic material and the axial moduli *M*$_0$//*a* and *M*$_0$//*c* are in a relative ratio between 1.28 : 1 (this study and anhydrous Al$_3$(Mg,Fe)$_2$AlSi$_5$O$_{18}$ [9], 1.22 : 1 in Be$_3$Al$_2$Si$_6$O$_{18}$ [44], and 1.18 : 1 CO$_2$-intercalated Al$_3$(Mg,Fe)$_2$AlSi$_5$O$_{18}$ [11]).

4.2. Stereochemistry of extra-framework guest atom at non-ambient P and T conditions

The electron density maps determined in this study confirm the distribution of the extra-framework atoms Cs and Na as determined by Ref. [16]. In line with the higher-order centrosymmetric $R\overline{3}c$ symmetry, these atoms occupy sites along the central three-fold axis of the channel, i.e. Cs1 on the Wyckoff positions 12*c* (point symmetry 3.), Cs2 on 6*a* (32),

Na1 on 6*b* ($\bar{3}$), and Na2 on 12*c* (3.) (Fig. 8). A full occupation of these sites would provide 1 Cs + 1 Na atom per formula unit. The actual refinements of the SOF's at 173 K, on the other hand, confirm that 73.0 ± 0.2% is occupied by Cs, and 13.5 ± 3.0% by Na.

However, a detailed examination of the electron-density distribution around these positions shows that the electron density around the Cs atoms is clearly displaced laterally, as already reported by Ref. [16], who interpreted the Cs atoms to be located directly at 0,0,*z* (*z* ≈ 1/12 for Cs1, ¼ for Cs2) and Ow1 and Ow2 of potential guest H_2O in the immediate vicinity off the tri-fold axis. . Ideally, the Cs sites lie on the central position of the channel, and thus on the triad (labeled Cs1* and Cs2* in Fig. 8). Since the central position Cs* always leads to too long Cs–O bond distances, the lateral displacement off the channel center line also seems to be justified by stereochemistry. Accordingly, Cs1 and Cs2 position were refined on general positions 36*f*, which are displaced at 173 K by ~0.007(2) Å (Cs1) to 0.095(8) Å (Cs2) from the ideal Cs* positions located at 12*c* and 6*a*, respectively. The resulting coordination polyhedra correspond to a [3 + 6+3] coordination with Cs1–O distances ranging from 3.28 to 3.50 Å, and a [6 + 6] coordination with Cs2–O distances from 3.28 to 3.75 Å (cf. Fig. 10).

The lateral displacement was not refined under high-*P*, so that the Cs atoms were modelled on the three-fold axis. However, due to the acentric symmetry in *R3c*, on two independent positions, i.e. Cs1*A* and Cs1*B* (Table S9, supplement). While the two Cs1 positions at 9.13 GPa still correspond to the earlier described [12]-fold coordination (cf. Fig. S9, supplement) with Cs–O distances 3.10–3.46 Å and 3.13–3.42 Å, the Cs2 atoms coordination changes to [6 + 9], however not only through additional 3 bonds to the O6 framework atoms. Instead there is a release of the three O9*B* atoms (Cs2–O9 at RT: 3.617(2) Å; Cs2–O9*B* at 9.13 GPa: 3.86(1) Å) and new bonding of all six O6*A* (Cs2–O6: 3.73(2) Å) and O6*B* atoms (Cs2–O6: 3.77(2) Å) from a former Cs2–O6 distance of 3.995(2) Å. The O9*A* atoms do not shift as much, changing from 3.617(2) Å at ambient conditions to 3.71(1) Å at 9.13 GPa. Interestingly, the O1 atoms, i.e. the atoms with the longest distance to the Cs2 atoms that could possibly be part of a coordination polyhedra (Fig. 10), also split up changing their distance from 4.098(2) Å at ambient conditions to 3.88(2) Å and 3.98(2) Å at 9.13 GPa (cf. Fig. 10). Anyway, this change of coordination from [6 + 6] to [6 + 9] is only possible in space group *R3c* and would change to a more unrealistic coordination of [6 + 6+6] for space group *R$\bar{3}$c*.

Displacive shifts can also be observed for part of the Na sites, i.e. for the Na2 position (as located on 12*c* in *R$\bar{3}$c*, now on two sites Na2*A* and Na2*B*, each located at 6*a*). In contrast to the Cs atoms, the Na atoms get displaced along the threefold axis while keeping coordinates 0,0,*z*. The bonding scheme is not changed significantly if compared to the findings of [16], who described it as [2 + 6] coordination, i.e. two bonds to the Ow atoms (Ow1, Ow2) located at the Cs* sites, completed by six Na–O bonds to the framework oxygen atoms O7, O8, and O9 (Fig. 8). Again, under pressure, the positions are shifted, but the coordination of Na is not changed if compared to the pressure-induced stereochemical changes of the Cs atoms.

The arrangement of the channel sites follows a sequence of alternating Na and Cs atoms, in an approximate sequence at *z* = 0, 1/12, 2/12, 3/12, …. Looking at the stereochemical possibilities and considering which positions can be occupied at the same time, there are only a few ordering schemes of the channel sites. This includes the sequence of [Cs1···Cs2···Cs1]$_n$, with CsO$_{12}$ face-sharing polyhedra along the *c*-axis (Fig. 9). In this case, it would be possible to achieve a fully stuffed channel according to SOF's of 1.0 at each of the three Cs sites in *R3c*. Na could also have full occupancy, requiring the additional Ow1 and Ow2 positions, which implies a given fraction of H_2O (Fig. 9). If the channels were exclusively filled with Na or Cs, there would be a full occupation of one alkali atom per formula unit. However, if one considers a mixed occupation by Na and Cs within a single channel, only a partial occupation of the Cs and Na positions is possible due to the limited possibilities for stereochemically meaningful bonds (cf. Fig. 8).

5. Conclusions

The present study shows that variation of *P* (at least up to 10 GPa) and *T* (at least up to 1200 K) leads to an apparently second-order displacive phase transition of (Cs,Na)[(Be$_2$Li)Al$_2$Si$_6$O$_{18}$] from *R$\bar{3}$c→R3c*, which does not influence the structural stability, despite its open-framework (beryl-type) structure.

Both the framework topology and the *R$\bar{3}$c* superstructure, due to (Li, Be) ordering scheme on [4]T1 sites, remain unaffected throughout the variations in *P* and *T* space. While the well-ordered framework is responsible for sharp Bragg reflections in the diffraction pattern corresponding to Laue class $\bar{3}m1$, disorder between adjacent one-dimensionally ordered arrangements of the channel population (i.e. Cs, Na and H_2O) is responsible for the appearance of detectable diffuse scattering. Since the diffuse scattering does not change in response to the applied *P* and *T*, it can be assumed that the order within the individual channels remains unaffected. Nevertheless, the investigations at low *T* and at the highest *P* show that deviations from the superordinate framework symmetry originate from displaced atom positions inside the channels, as required for adaption of individual bonds. Therefore, the centrosymmetry is broken and the structure is slightly distorted by cooperative atomic displacements in accordance with the acentric space group *R3c*. The resulting *R$\bar{3}$c-to-R3c* phase transformation is relatively inconspicuous, recognizable in the measurements towards low-*T* conditions but most pronounced in the compressed structure. Hints for the subtle transformation can be found in: individual Raman modes in the region of the external vibrations, in lower residuals of refinements of the structures in the non-centrosymmetric space group *R3c*, but also in the behavior of the unit-cell parameters in connection with the thermal expansion or with isothermal compression. The critical transition point for the *T* space was found to be at *T*$_c$ = 312 ± 5 K, while the *P*$_c$ seems to be in a region between 2.8 and 5.3 GPa. The description of the crystal structure in a correspondingly twinned acentric polymorph is a new aspect compared to previous findings on this stuffed beryl-type structure. Both the aspects of structural stability under the *P*, *T* variations carried out in this study and the thermomechanical properties* confirm that this class of material has a high potential for technical application [*low thermal expansion coefficient, high resistance to thermal shocks, a pronounced structural stability at high-*T* and high-*P* conditions (all typical for beryl type framework structures), less pronounced anisotropy of thermal expansion (compared to other beryl type framework structures), a negative thermal expansion value in the *a*-axis direction at *T* < 300 K (first time observed for a beryl type framework structure)]. If a simple synthesis route of this material will be developed, for example under hydrothermal conditions, the anhydrous end-member Cs[(Be$_2$Li)Al$_2$Si$_6$O$_{18}$] would serve as a potential solid hosts for [137]Cs γ-radiation source in sterilization applications. The low amount of potential contained Cs (up to 19.9 wt% for the anhydrous endmember) likely makes this material not an ideal candidate for use in the immobilization of radioactive Cs-isotopes, though the Cs-retention under extreme conditions, especially at high-*T*, in a crystalline structure makes it suitable for this type of utilizations.

CRediT authorship contribution statement

Martin Ende: Investigation, Formal analysis, Conceptualization, Visualization, Writing - review & editing. **G. Diego Gatta:** Resources, Investigation, Writing - review & editing. **Paolo Lotti:** Investigation, Writing - review & editing. **Alexander Grandtner:** Investigation, Formal analysis. **Ronald Miletich:** Conceptualization, Writing - original draft, Writing - review & editing.

Declaration of competing interest

Acknowledgments

Appendix A. Supplementary data

Supplementary data to this article can be found online at https://doi.org/10.1016/j.jssc.2020.121841.

References

[1] R.I. Mashkovtsev, V.G. Thomas, Nitrogen atoms encased in cavities within the beryl structure as candidates for qubits. Appl. Magn. Reson., Springer, New York, 2005, pp. 401–409, https://doi.org/10.1007/BF03166771.

[2] C. Sanchez-Valle, C.H. Chio, G.D. Gatta, Single-crystal elastic properties of (Cs,Na) AlSi$_2$O$_6$H$_2$O pollucite: a zeolite with potential use for long-term storage of Cs radioisotopes, J. Appl. Phys. 108 (2010), 093509, https://doi.org/10.1063/1.3504613.

[3] B.P. Gorshunov, V.I. Torgashev, E.S. Zhukova, V.G. Thomas, M.A. Belyanchikov, C. Kadlec, F. Kadlec, M. Savinov, T. Ostapchuk, J. Petzelt, J. Prokleška, P.V. Tomas, E.V. Pestrjakov, D.A. Fursenko, G.S. Shakurov, A.S. Prokhorov, V.S. Gorelik, L.S. Kadyrov, V.V. Uskov, R.K. Kremer, M. Dressel, Incipient ferroelectricity of water molecules confined to nano-channels of beryl, Nat. Commun. 7 (2016), https://doi.org/10.1038/ncomms12842.

[4] G.D. Gatta, A. Brundu, P. Cappelletti, G. Cerri, B. de' Gennaro, M. Farina, P. Fumagalli, L. Guaschino, P. Lotti, M. Mercurio, New insights on pressure, temperature, and chemical stability of CsAlSi$_5$O$_{12}$, a potential host for nuclear waste, Phys. Chem. Miner. 43 (2016) 639–647, https://doi.org/10.1007/s00269-016-0823-8.

[5] G.D. Gatta, P. Lotti, G. Tabacchi, The effect of pressure on open-framework silicates: elastic behaviour and crystal–fluid interaction, Phys. Chem. Miner. 45 (2018) 115–138, https://doi.org/10.1007/s00269-017-0916-z.

[6] G.D. Gatta, F. Nestola, G.D. Bromiley, S. Mattauch, The real topological configuration of the extra-framework content in alkali-poor beryl: a multi-methodological study, Am. Mineral. 91 (2006) 29–34, https://doi.org/10.2138/am.2006.1896.

[7] T. Armbruster, E. Libowitzky, M. Auernhammer, P. Bauerhansl, C. Hoffmann, E. Irran, A. Kurka, H. Rosenstingl, L. Diamond, Crystal chemistry and optics of bazzite from Furkabasistunnel (Switzerland), Mineral. Petrol. 52 (1995) 113–126, https://doi.org/10.1007/BF01163130.

[8] G. Della Ventura, P. Rossi, G.C. Parodi, A. Mottana, M. Raudsepp, M. Prencipe, Stoppaniite, (Fe,Al,Mg)$_4$(Be$_6$Si$_{12}$O$_{36}$)*(H$_2$O)$_2$(Na,□) a new mineral of the beryl group from Latium (Italy), Eur. J. Mineral 12 (2000) 121–127, https://doi.org/10.1127/0935-1221/2000/0012-0121.

[9] R. Miletich, K.S. Scheidl, M. Schmitt, A.P. Moissl, T. Pippinger, G.D. Gatta, B. Schuster, C. Trautmann, Static elasticity of cordierite I: effect of heavy ion irradiation on the compressibility of hydrous cordierite, Phys. Chem. Miner. 41 (2014) 579–591, https://doi.org/10.1007/s00269-014-0671-3.

[10] R. Miletich, G.D. Gatta, T. Willi, P.W. Mirwald, P. Lotti, M. Merlini, N. Rotiroti, T. Loerting, Cordierite under hydrostatic compression: anomalous elastic behavior as a precursor for a pressure-induced phase transition, Am. Mineral. 99 (2014) 479–493, https://doi.org/10.2138/am.2014.4487.

[11] K.S. Scheidl, G.D. Gatta, T. Pippinger, B. Schuster, C. Trautmann, R. Miletich, Static elasticity of cordierite II: effect of molecular CO$_2$ channel constituents on the compressibility, Phys. Chem. Miner. 41 (2014) 617–631, https://doi.org/10.1007/s00269-014-0675-z.

[12] B. Charoy, P. De Donato, O. Barres, C. Pinto-Coelho, Channel occupancy in an alkali-poor beryl from serra branca (goias, Brazil): spectroscopic characterization, Am. Mineral. 81 (1996) 395–403, https://doi.org/10.2138/am-1996-3-414.

[13] B.M. Laurs, W.B. Skip Simmons, G.R. Rossman, E.P. Quinn, S.F. McClure, A. Peretti, T. Armbruster, F.C. Hawthorne, A.U. Falster, D. Günther, M.A. Cooper, B. Grobéty, Pezzottaite from ambatovita, Madagascar: a new gem mineral, Gems Gemol. 39 (2003) 284–301, https://doi.org/10.5741/gems.39.4.284.

[14] F.C. Hawthorne, M.A. Cooper, W.B. Simmons, A.U. Falster, B.M. Laurs, T. Armbruster, G.R. Rossman, A. Peretti, D. Günter, B. Grobéty, Pezzottaite Cs(Be$_2$Li)Al$_2$Si$_6$O$_{18}$ A spectacular new beryl-group mineral from the Sakavalana pegmatite, Fianarantsoa province, Madagascar, Mineral. Rec. 35 (2004) 369–378.

[15] S.I. Liu, M.S. Peng, A new gem mineral. The vibrational spectroscopic characterization of pezzottaite, Acta Mineral. Sin. 25 (2005) 60–64.

[16] O.V. Yakubovich, I.V. Pekov, I.M. Steele, W. Massa, N.V. Chukanov, Alkali metals in beryl and their role in the formation of derivative structural motifs: comparative crystal chemistry of vorobyevite and pezzottaite, Crystallogr. Rep. 54 (2009) 399–412, https://doi.org/10.1134/s1063774509030067.

[17] G.G. Panczer, D. Ligny, M. Boudeulle, B. Champagnon, Luminescent centres in pezzottaite, CsBe$_2$LiAl$_2$Si$_6$O$_{18}$, Eur. J. Mineral 22 (2010) 605–612, https://doi.org/10.1127/0935-1221/2010/0022-2039.

[18] G.D. Gatta, I. Adamo, M. Meven, E. Lambruschi, A single-crystal neutron and X-ray diffraction study of pezzottaite, Cs(Be$_2$Li)Al$_2$Si$_6$O$_{18}$, Phys. Chem. Miner. 39 (2012) 829–840, https://doi.org/10.1007/s00269-012-0539-3.

[19] E. Lambruschi, G.D. Gatta, I. Adamo, D. Bersani, E. Salvioli-Mariani, P.P. Lottici, Raman and structural comparison between the new gemstone pezzottaite Cs(Be$_2$Li) Al$_2$Si$_6$O$_{18}$ and Cs-beryl, J. Raman Spectrosc. 45 (2014) 993–999, https://doi.org/10.1002/jrs.4479.

[20] G.J. Finkelstein, P.K. Dera, T.S. Duffy, High-pressure phases of cordierite from single-crystal X-ray diffraction to 15 GPa, Am. Mineral. 100 (2015) 1821–1833, https://doi.org/10.2138/am-2015-5073.

[21] M.A. Camerucci, G. Urretavizcaya, M.S. Castro, A.L. Cavalieri, Electrical properties and thermal expansion of cordierite and cordierite-mullite materials, J. Eur. Ceram. Soc. 21 (2001) 2917–2923, https://doi.org/10.1016/S0955-2219(01)00219-9.

[22] R. Miletich, D.R. Allan, W.F. Kuhs, High-pressure single-crystal techniques, Rev. Mineral. Geochem. 41 (2000) 445–519, https://doi.org/10.2138/rmg.2000.41.14.

[23] R.J. Angel, D.R. Allan, R. Miletich, L.W. Finger, The use of quartz as an internal pressure standard in high-pressure crystallography, J. Appl. Crystallogr. 30 (1997) 461–466, https://doi.org/10.1107/S0021889897000861.

[24] S.D. Jacobsen, C.M. Holl, K.A. Adams, R.A. Fischer, E.S. Martin, C.R. Bina, J.F. Lin, V.B. Prakapenka, A. Kubo, P. Dera, Compression of single-crystal magnesium oxide to 118 GPa and a ruby pressure gauge for helium pressure media, Am. Mineral. 93 (2008) 1823–1828, https://doi.org/10.2138/am.2008.2988.

[25] K.S. Scheidl, R. Miletich, A. Kurnosov, D.M. Trots, T. Boffa Ballaran, R.J. Angel, Extending the single-crystal quartz pressure gauge up to hydrostatic pressure of 19 GPa, J. Appl. Crystallogr. 49 (2016) 2129–2137, https://doi.org/10.1107/S1600576716015351.

[26] R. Angel, J. Gonzalez-Platas, *ABSORB-7* and *ABSORB-GUI* for single-crystal absorption corrections, J. Appl. Crystallogr. 46 (2013) 252–254, https://doi.org/10.1107/S0021889812048431.

[27] E. Prince, International Tables for Crystallography Volume C: Mathematical, Physical and Chemical Tables, International Union of Crystallography, Chester, England, 2006, https://doi.org/10.1107/97809553602060000103.

[28] G.M. Sheldrick, Crystal structure refinement with SHELXL, Acta Crystallogr. C 71 (2015) 3–8, https://doi.org/10.1107/S2053229614024218.

[29] C.B. Hübschle, G.M. Sheldrick, B. Dittrich, ShelXle, A Qt graphical user interface for SHELXL, J. Appl. Crystallogr. 44 (2011) 1281–1284, https://doi.org/10.1107/S0021889811043202.

[30] R.J. Angel, L.W. Finger, SINGLE : a program to control single-crystal diffractometers, J. Appl. Crystallogr. 44 (2011) 247–251, https://doi.org/10.1107/S0021889810042305.

[31] H.E. King, L.W. Finger, Diffracted beam crystal centering and its application to high-pressure crystallography, J. Appl. Crystallogr. 12 (1979) 374–378, https://doi.org/10.1107/S0021889879012723.

[32] J. Gonzalez-Platas, M. Alvaro, F. Nestola, R. Angel, IUCr, EosFit7-Gui, A new graphical user interface for equation of state calculations, analyses and teaching, J. Appl. Crystallogr. 49 (2016) 1377–1382, https://doi.org/10.1107/S1600576716008050.

[33] A. Le Bail, H. Duroy, J.L. Fourquet, Ab-initio structure determination of LiSbWO6 by X-ray powder diffraction, Mater. Res. Bull. 23 (1988) 447–452, https://doi.org/10.1016/0025-5408(88)90019-0.

[34] B.H. Toby, EXPGUI, a graphical user interface for GSAS, J. Appl. Crystallogr. 34 (2001) 210–213, https://doi.org/10.1107/S0021889801002242.

[35] B.H. Toby, R.B. Von Dreele, GSAS-II: the genesis of a modern open-source all purpose crystallography software package, J. Appl. Crystallogr. 46 (2013) 544–549, https://doi.org/10.1107/S0021889813003531.

[36] A.M. Hofmeister, T.C. Hoering, D. Virgo, Vibrational spectroscopy of beryllium aluminosilicates: heat capacity calculations from band assignments, Phys. Chem. Miner. 14 (1987) 205–224, https://doi.org/10.1007/BF00307985.

[37] C.C. Kim, M.I. Bell, D.A. McKeown, Vibrational analysis of beryl (Be$_3$Al$_2$Si$_6$O$_{18}$) and its constituent ring (Si$_6$O$_{18}$), Phys. B Phys. Condens. Matter. 205 (1995) 193–208, https://doi.org/10.1016/0921-4526(94)00290-C.

[38] I. Moroz, M. Roth, M. Boudeulle, G. Panczer, Raman microspectroscopy and fluorescence of emeralds from various deposits, J. Raman Spectrosc. 31 (2000) 485–490, https://doi.org/10.1002/1097-4555(200006)31:6<485::AID-JRS561>3.0.CO, 2-M.

[39] R.G. Berman, Internally-consistent thermodynamic data for minerals in the system Na$_2$O-K$_2$O-CaO-MgO-FeO-Fe$_2$O$_3$-Al$_2$O$_3$-SiO$_2$-TiO$_2$-H$_2$O-CO$_2$, J. Petrol. 29 (1988) 445–522, https://doi.org/10.1093/petrology/29.2.445.

[40] D. Kuscer, I. Bantan, M. Hrovat, B. Malič, The microstructure, coefficient of thermal expansion and flexural strength of cordierite ceramics prepared from alumina with different particle sizes, J. Eur. Ceram. Soc. 37 (2017) 739–746, https://doi.org/10.1016/j.jeurceramsoc.2016.08.032.

[41] B. Morosin, Structure and thermal expansion of beryl, Acta Crystallogr. B 28 (1972) 1899–1903, https://doi.org/10.1107/s0567740872005199.

[42] P.W. Mirwald, Thermal expansion of anhydrous Mg-cordierite between 25 and 950° C, Phys. Chem. Miner. 7 (1981) 268–270, https://doi.org/10.1007/BF00311979.

[43] M.F. Hochella, G.E. Brown, Structural mechanisms of anomalous thermal expansion of cordierite-beryl and other framework silicates, J. Am. Ceram. Soc. 69 (1986) 13–18, https://doi.org/10.1111/j.1151-2916.1986.tb04685.x.

[44] D. Fan, J. Xu, Y. Kuang, X. Li, Y. Li, H. Xie, Compressibility and equation of state of beryl ($Be_3Al_2Si_6O_{18}$) by using a diamond anvil cell and in situ synchrotron X-ray diffraction, Phys. Chem. Miner. 42 (2015) 529–539, https://doi.org/10.1007/s00269-015-0741-1.

[45] E. O'Bannon, Q. Williams, Beryl-II, a high-pressure phase of beryl: Raman and luminescence spectroscopy to 16.4 GPa, Phys. Chem. Miner. 43 (2016) 671–687, https://doi.org/10.1007/s00269-016-0837-2.

[46] F. Birch, Finite elastic strain of cubic crystals, Phys. Rev. 71 (1947) 809–824, https://doi.org/10.1103/PhysRev.71.809.

[47] M.I. Aroyo, J.M. Perez-Mato, C. Capillas, E. Kroumova, S. Ivantchev, G. Madariaga, A. Kirov, H. Wondratschek, Bilbao Crystallographic Server: I. Databases and crystallographic computing programs, Z. Krist.-Cryst. Mater. 221 (2006) 15–27, https://doi.org/10.1524/zkri.2006.221.1.15.

[48] M.I. Aroyo, J.M. Perez-Mato, D. Orobengoa, E. Tasci, G. de la Flor, Crystallography online: Bilbao crystallographic server, Bulg. Chem. Commun. 43 (2011) 183–197.

[49] G. De La Flor, D. Orobengoa, E. Tasci, J.M. Perez-Mato, M.I. Aroyo, Comparison of structures applying the tools available at the Bilbao Crystallographic Server, J. Appl. Crystallogr. 49 (2016) 653–664, https://doi.org/10.1107/S1600576716002569.

[50] S. Parsons, H.D. Flack, T. Wagner, Use of intensity quotients and differences in absolute structure refinement, Acta Crystallogr. B-Stru. 69 (2013) 249–259, https://doi.org/10.1107/S2052519213010014.

[51] S. Parsons, Introduction to twinning, Acta Crystallogr. D 59 (2003) 1995–2003, https://doi.org/10.1107/S0907444903017657.

[52] E. Kroumova, M.I. Aroyo, J.M. Perez-Mato, A. Kirov, C. Capillas, S. Ivantchev, H. Wondratschek, Bilbao crystallographic Server : useful databases and tools for phase-transition studies, Phase Transitions 76 (2003) 155–170, https://doi.org/10.1080/0141159031000076110.